Modification of the wake of a wall-mounted bathymetry obstacle submitted to waves opposing a tidal current

Magnier Maëlys [1], Saouli Yanis [1], Gaurier Benoît [1], Druault Philippe [2], Germain Grégory [1, *]

[1] Ifremer, Marine Structure Laboratory, 150 Quai Gambetta 62200 Boulogne sur Mer, France
[2] Sorbonne Université, CNRS, UMR 7190, Institut Jean Le Rond d'Alembert, F-75005 Paris, France

* Corresponding author : Grégory Germain, email address : gregory.germain@ifremer.fr

Abstract :

In this paper, the effects of regular waves propagating against the current on the wake of a wide bathymetric obstacle are experimentally investigated. For that purpose, a square cylinder of height representing of the water column, mounted perpendicular to the flow, is used. Both Reynolds and Froude numbers are close to the ones encountered at sea and swell properties (amplitude, frequency and wavelength) which are typical conditions in the English Channel. To study this complex hydrodynamic interaction, PIV measurements are used to capture the velocity field around and in the wake of the cylinder. The wake of this wide cylinder has been extensively studied and is characterised by its direction towards the water surface and by energetic and wide vortices arising from the sheared layer at a Strouhal number of approximatively 0.06, after a merging of smaller eddies. In this work, the focus is on how surface gravity waves, propagating against the current, modify the generation of these turbulent structures. The results show that the cylinder wake is strongly modified in the presence of waves, even if, on average, the main wake structure is globally conserved. The waves act both on the vortex generation and the wake development with modifications in terms of turbulent energy distribution and level, wake recovery and ascent rate. The vortex shedding becomes highly energetic and well-organised from the cylinder position. Its return period is extremely regular and corresponds to half of the wave frequency which is really close to the natural vortex shedding frequency. That results in a doubling of the statistical length scale of the vortices.

Highlights

► Swell induced-motion effects on high and isolated bathymetry roughness. ► Bottom mounted cylinder wake characterisation in presence of waves opposing current. ► Vortex generation and dynamic study. ► Energy transfer between wave and vortex shedding frequency in the near-wake.

Keywords : Obstacle, Wave, Wake, Vortex, Turbulence

1 Introduction

High-potential tidal energy sites are characterised by strong tidal currents. They are turbulent and sheared due to their interaction with bathymetric obstacles. At those sites, surface gravity waves are also often present, especially in winter (Filipot et al. 2015; Bennis et al. 2022). They are either wind seas short and low-energy waves or long and energetic swells from offshore, generated by storm winds.

Turbulent tidal currents and surface gravity waves interact together to create complex hydrodynamic conditions, both spatially and temporally. The behaviour of the tidal current is thus modified: mean velocity profiles and turbulent characteristics are altered by the wave motions, while the wave kinematics are modified by the current (Zhang et al. 2022). Rey et al.

(2014) and Barman et al. (2016) show that, in coastal areas, the wake of wall-mounted obstacles, representing bathymetry, is modified by surface gravity waves which in turn are altered by the obstacles presence. In similar conditions, without bathymetric obstacles, surface gravity waves also organised the random turbulent fluctuations of the flow depending on the wave frequency (Roy et al. 2017; Roy et al. 2018). In addition, Chen et al. (2014) show that the presence of waves following the current leads to the generation of vortices in the wake of a parabolic obstacle. However, all those studies have been conducted at coastal area scale, with the bathymetric obstacle representing half of the water depth.

At tidal energy sites, obstacles are smaller compared to the water depth. For example, in the Alderney Race, a high potential energetic site of the English Channel, the higher bathymetric obstacles represent approximately $1/8^{\text{th}}$ of the water column. In those areas, the order of magnitude of the average wavelength is 100 m, which is more than twice the depth, and the average peak period is around 11 s (Furgerot et al. 2020; Bennis et al. 2022). Thanks to previous studies carried out in the Ifremer wave and current flume tank among others, it has been shown that a wide bottom-mounted cylinder set perpendicular to the flow correctly represents the bathymetry-current interaction. It generates an energetic wake, directed towards the surface, in which energetic vortices are released at $St \approx 0.07$, after a vortex merging time (Ikhennicheu et al. 2019). Two preliminary studies covering a wide range of wave cases following or opposing the current have been conducted in our laboratory in Froude similarity to Alderney Race. Magnier et al. (2022) highlight cylinder wake modifications caused by waves following the current if their frequency is low enough. Saouli et al. (2022) cover a wide range of frequency and amplitude of waves opposing the current. As for waves with the current, low-frequency waves are the most impacting on the cylinder wake. Turbulent kinetic energy spikes appear in some precise and key positions in the wake or above the cylinder, and the vortex shedding focuses on the multiple of the wave frequency.

The aim of this study is to understand thoroughly how the surface gravity waves modify the vortex generation resulting from the bathymetry–current interaction in tidal energy sites. The experiments are carried out using the bottom-mounted square cylinder presented above. The wave case is chosen to be the most representative of the English Channel conditions. The wake of the cylinder, under this opposing current wave case, is compared to its reference wake, generated in calm sea conditions. Time-resolved Particle Image Velocimetry is used to measure the flow fields in the symmetry plane of the cylinder. The paper is structured as follows. First, the experimental setup is presented. A basic physical wave description, including both the description of the water surface shape and the water motion below the surface, is given. Then, the effects of the surface gravity waves on the dynamics of the cylinder wake are studied using time-averaged velocities and Reynolds tensor maps, temporal and spectral analysis of the velocity, and statistical correlation and estimation of the turbulent flow vortex size. Finally, phase averaging is performed at the vortex shedding frequency to discuss about the vortex generation and the modification of the wake development due to the waves.

2 Experimental setup

2.1 Current, wave and bathymetry modelisation in the flume tank

Tests are carried out in the wave and current circulating tank of IFREMER located in Boulogne-sur-Mer (France). The test section is 20 m long $\times$ 4 m wide $\times$ 2 m deep (see Figure 1). The incoming flow $(U_\infty, V_\infty, W_\infty)$ is assumed to be steady and constant, with the imposed velocity: $U_\infty = 0.8$ m.s^{-1} and $V_\infty = W_\infty = 0$ m.s^{-1}. The three instantaneous velocity components are denoted (U, V, W) along the (x, y, z) directions respectively. According to the Reynolds decomposition, each instantaneous velocity component is separated into a mean value

and a fluctuating part: $U = \overline{U} + u'$ where the over-bar indicates the time averaging. Thanks to a grid combined with a honeycomb placed at the inlet of the working section, a low turbulence intensity $I_\infty = 1.5$ % is reached (Ikhennicheu et al. 2019) and the boundary layer height, calculated as follows $\delta_{95} = z \ (\overline{U} = 0.95 \times U_\infty)$, is equal to $\delta_{95} \approx 0.25$ m.
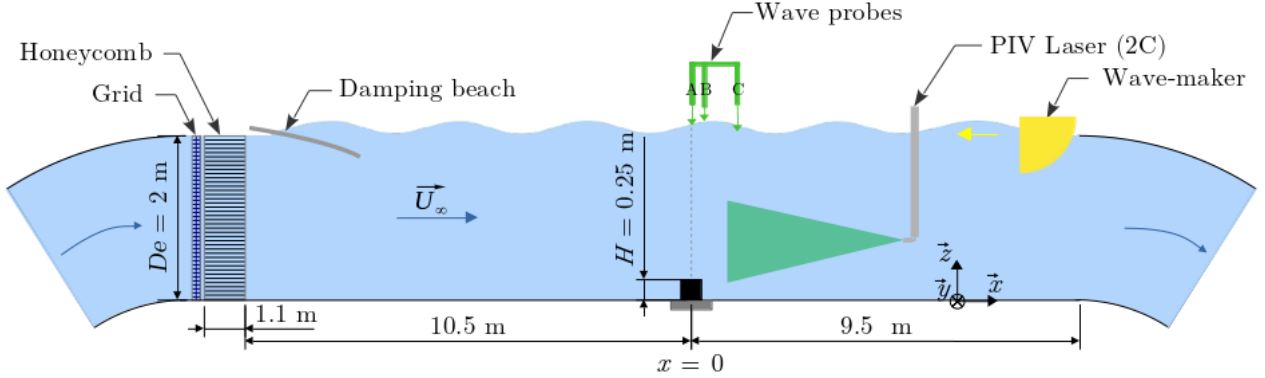

Figure 1: Sketch of the flow configuration showing the cylinder and the 3 wave probes locations, the PIV laser sheet, and the wave-maker at the outlet of the test section. The current comes from the left and the surface gravity waves from the right.

To generate waves at the flume tank surface, a wave generator is used. In this experiment, it is set at the outlet of the working section of the tank, as shown in Figure 1 and Figure 2. The wave generator is composed of 8 independent displacement paddles each 50 cm wide and 50 cm deep. At $U_\infty = 0.8$ m.s^{-1}, the capabilities of the wave generator enable the production of regular waves with a frequency range between $f = 0.2$ Hz and $f = 0.6$ Hz and a maximum amplitude of $A = 150$ mm (from still water level to crest). At the inflow of the working section, a damping beach, made of a metallic porous panel (8% porosity), is set to reduce as much as possible wave reflection on the inlet wall of the tank. Measurements revealed that the resulting reflection coefficient was lower than 12% for all the usual frequencies and amplitudes. Wave spectrum models (Pierson-Moskowitz, JONSWAP, Bretschneider, and others) can be used for the generation of random waves (Gaurier et al. 2010).
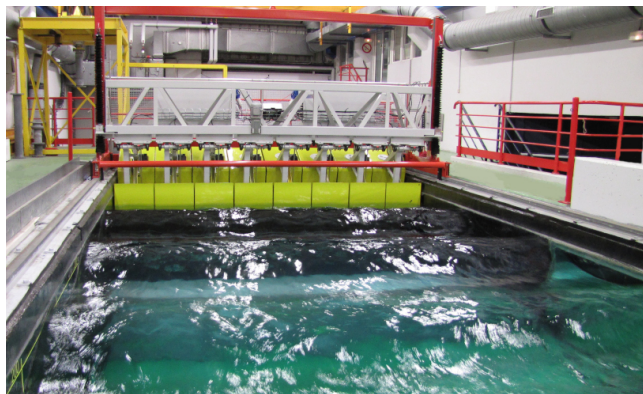

Figure 2: Regular waves with a 0.8 m/s flow in the Ifremer current flume tank

To represent at scale a large seabed roughness, a square cylinder of section $H \times H$, with $H = 0.25$ m, and of width $6H$ is used, as presented in Figure 3. The $x-$origin is set at the centre of the cylinder. $z = 0$ corresponds to the tank floor. The square cylinder is centred in the spanwise direction of the tank. Spanwise origin ($y = 0$) is set to the centre of the square cylinder (Figure 1).

Figure 3: PIV setup with the camera in foreground and the laser sheet illuminating the square cylinder. The resistive wave probes are passing through the free-surface where a wave-trough is visible on top of the cylinder.

The present investigation is conducted in geometrical similitude 1:20 to real sea conditions (Ikhennicheu et al. 2019), for which the Alderney Race conditions has been considered. Then, the incoming flow Reynolds number based on the cylinder height is $Re_H = HU_\infty/\nu = 2.0 \times 10^5$ with ν the water kinematic viscosity. The Froude number is equal to $Fr = U_\infty/\sqrt{g \times D_e} = 0.18$, with D_e the flume tank depth and g the gravity. The scaled experiment parameters are presented in Table 1.

	Scale	U_∞ [m/s]	Rugosity H [m]	Depth D_e [m]	$Re_H = \frac{HU_\infty}{\nu}$	$Fr = \frac{U_\infty}{\sqrt{g \times D_e}}$
Alderney Race	1	3.5	5	40	1.8×10^7	0.18
Flume tank	1/20	0.8	0.25	2	2.0×10^5	0.18

Table 1: In-situ and experimental hydrodynamic conditions (1:20 scale).
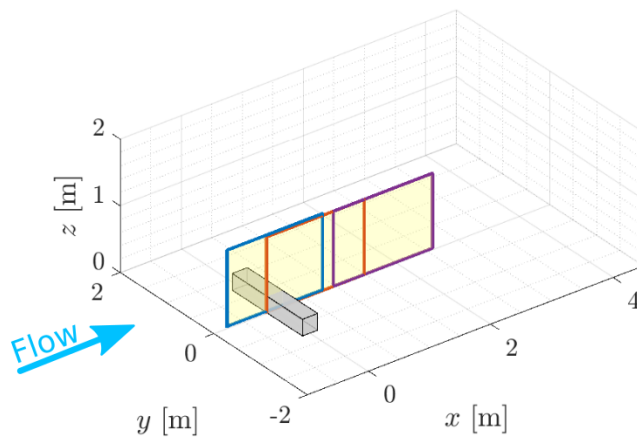
2.2 Measurement tools

Figure 4: Sketch of PIV measurement planes configuration

To characterise the flow, 2D Particle Image Velocimetry (PIV) measurements are conducted in the symmetry plane of the cylinder, at $y = 0$ (see Figure 3). This enables $U(x, z, t)$ and

$W(x, z, t)$ in plane Oxz to be accessed. To capture the entire cylinder wake, three measurement planes are selected along the x-axis. Figure 4 presents their spatial positions. They are acquired successively using the same camera, which is translated along the x-direction behind the big lateral window of the tank (see figure 3). The image stitching between the three measurement planes is done manually knowing the displacement between the plane along the x-axis (y and z positions remains the same). Due to the use of a wide angle camera and the slight window unevenness, a distortion is observed on the edge of the field. This distortion generates a velocity modification lower than 2% in the corners, which are mostly removed on the present results. This explains the small gaps that can be observed between two measurement planes in stitched velocity maps shown on the following sections. Before PIV measurements, the tank is seeded with 10 µm diameter silver-coated glass micro-particles. Particles illuminated by a 200 mJ Nd-Yag laser are detected on 4 to 10 pixels. To process PIV images, the software *Dynamic studio* is used. The displacement of particles is calculated using the Adaptive PIV method on 32 pix x 32 pix interrogation windows. Outliers are replaced using the Universal Outlier Detection method (Westerweel et al. 2005). PIV acquisitions are carried out during 200 s, hence 3000 double images are taken at 15 Hz acquisition frequency. The time between a double-frame is equal to $\Delta t = 900$ µs, excepted for data presented in section 2.3 where $\Delta t = 8000$ µs for flow measurements without any wake interaction and due to experimental proceeding improvements. Measurement plane dimensions are 1.60 m×1.12 m with a spatial resolution of $dx = dz = 20$ mm.

The surface elevation is also measured with a combination of KENEK servo-type wave probes (model SHT3-30E) and resistive wave probes. The dynamic wave probe (denoted A in Figure 1) is set on top of the cylinder, at $(x, y) = (0, 0)$ m. Two resistive probes are set downstream, on positions B and C on the flume tank scheme, with $AB = 52$ cm and $BC = 70$ cm, in order to measure precisely the wave characteristics.

Finally, the wave probes are synchronised with the PIV system which triggers the start of the measurements. In the wave case, the measurements are started when the wave-current interaction has reached its equilibrium and when the conditions are stationary.

2.3 Input flow characterisation

To study the effects of surface gravity waves on the cylinder wake, two flow conditions are considered: a reference case with *current only*, which is compared to a case *with waves* propagating against the current. To characterise the imposed conditions, this section provides a basic physical description of the flow in the water column and at the free surface, compared to the reference case.

2.3.1 Wave conditions at the free surface

First, the wave case is described from the surface point of view, to compare it to wave properties at sea. To do so, the elevation of the water surface of the flume tank is measured with the three wave probes during 200 s. The measurement is made when the wave-current interaction has found its equilibrium (approximately 1 min after the beginning of the wave generation) and without the cylinder. In this wave case, the wave properties are stable in time and bi-dimensional (invariant along the y-direction). The main properties are presented in Table 2. The waves are characterised in time by f_h, which is the frequency at which waves are generated and is equal to 0.406 Hz. The parameter $\overline{A_{O1}}$ is the time-averaged wave amplitude at the wave frequency. This parameter is calculated by taking the time average of the amplitude of the Hilbert transform of the surface elevation signal, given by wave probe A, filtered around the wave frequency f_h. The height, from crest to trough of the waves, is defined as $H_{O1} = 2\overline{A_{O1}}$. The wavelength λ links time to space and is directly calculated using wave probes phase difference.

The celerity of the waves, which is the velocity at which the wave crests propagate, is defined as $C_\varphi = \lambda f_h$. Two non-dimensional parameters are also defined to characterise the type of wave conditions: H_{O1}/D_e is the relative height and λ/D_e is the relative wavelength. As $H_{O1}/D_e << 1$ and $2 < \lambda/D_e < 20$, the generated waves are of small height, linear with a finite depth. Airy theory can thus be used (Bougis 1993). Moreover, as $D_e < \lambda/2$, the wave-induced periodical velocity fluctuations are perceived right down to the bottom.

Concerning sea conditions in the English Channel, Furgerot et al. (2020) show that in the Alderney Race, the average significant wave height H_s is equal to 1.3 m and that H_s is included in $[0:5]$ m. Those events mainly come from the West with peak period T_p between 10 s and 16 s. Off the coast of Paimpol and Bréhat Island, another high potential tidal energy site of the English Channel, Moreau et al. (2022) showed that the most important wave events come from North-West with a peak period of about 12 s. The median significant wave height is equal to 1.15 m. At that site, waves propagate against ebb tide current and following flood current. Moreover, as shown in Bennis et al. (2022), in the Alderney Race, during winter storms, wavelengths can reach about 100 m, which is increased or decreased by the presence of ebb or flood currents (respectively). To compare our lab conditions to in-situ conditions, Table 2 presents the properties of the equivalent wave at sea, calculated using the scale factor 1/20 defined in Table 1. With a significant wave height (H_s) equal to 3.0 m, a peak period equal to 11 s and a wavelength equal to 98 m, this wave case represents severe wave conditions in the English Channel.

Wave case in the flume tank						At sea scale		
f_h [Hz]	A_{O1} [cm]	λ [m]	C_φ [m/s]	H_{O1}/D_e [-]	λ/D_e [-]	H_s [m]	T_p [s]	λ_{sea} [m]
0.406	7.6	4.9	2.0	0.076	2.5	3.0	11	98

Table 2: Main characteristics, in the flume tank and at sea scale, of the wave conditions.

2.3.2 Flow properties in the water column

Thanks to PIV measurements, the flow kinematics are studied for *current only* and current *with waves* cases, along a vertical profile at the centre of the test section $(x,y) = (0,0)$. In the following results, the reference velocity $U_{ref} = \overline{U(z = 0.5 \text{ m})}$ is used to normalise all velocity fields.

$$U^*(x,z,t) = \frac{U(x,z,t)}{U_{ref}} \quad \text{and} \quad W^*(x,z,t) = \frac{W(x,z,t)}{U_{ref}}$$

In the current only case, the reference velocity at $z = 0.5$ m is equal to $U_{ref} = 0.78$ m/s while it is equal to $U_{ref} = 0.85$ m/s with waves. This difference in velocity is due to the addition of the damping beach and the wave-maker, which reduces the available cross-sectional area and accelerates the flow for a given pump speed. The reference velocities U_{ref} are also used to calculate Strouhal numbers later.

Figure 5 presents the normalised mean velocity profiles in both cases. On the left-hand sub-figure, the $\overline{U^*(z)}$ profiles are superimposed for $z < 1.0$ m, i.e. over most of the water column studied here. Below $z \approx H = 0.25$ m, the velocity profiles show a classical boundary layer shape. Above, the mean streamwise velocity is constant and equal to U_{ref}. Higher than $z = 1.0$ m, the velocity profile shows a different behaviour depending on cases. For the wave case, the presence of the damping beach (upstream from the measurement area) generates fluctuations and decreases the velocity close to the free surface. Moreover, the waves, while propagating, interact with the current which induces modification of the velocity profile in the

upper part of the water column. In addition, $\overline{W^*(z)}$ is so small that it is considered equal to zero over the whole water column.
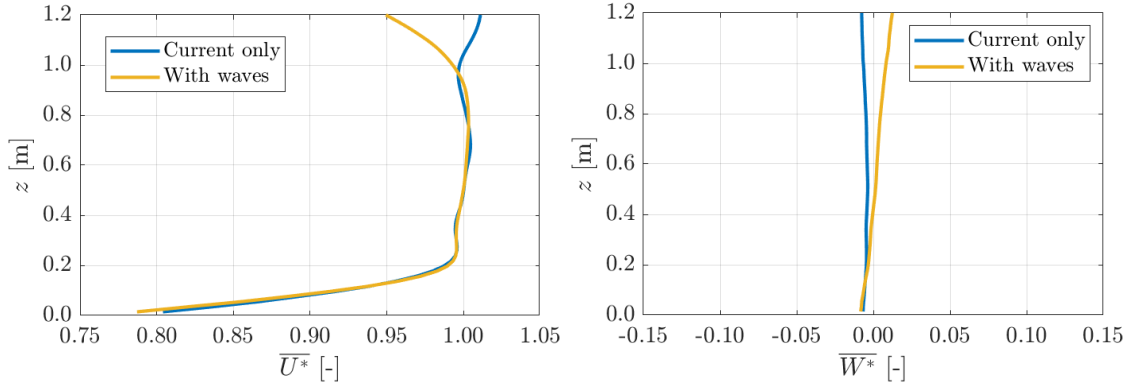

Figure 5: Normalised mean streamwise velocity $\overline{U^*(z)}$ profiles (left) and normalised mean vertical velocity $\overline{W^*(z)}$ profiles (right) at $(x, y) = (0, 0)$ m.

To estimate the turbulent intensity, the Reynolds decomposition of a given velocity signal under the influence of surface gravity waves is calculated as:

$$U(z, t) = \overline{U(z)} + u'(z, t) = \overline{U(z)} + u''(z, t) + \widetilde{u}(z, t)$$

where $\overline{U(z)}$ is the mean velocity, $u''(z, t)$ the turbulent fluctuations and $\widetilde{u}(z, t)$ is the regular and periodic component of the velocity fluctuation at the wave frequency f_h (Kemp et al. 1981; Perez et al. 2020). It is a sinus calculated with the ordinary least squares method. In the current only case, $\widetilde{u}(z, t) = 0$ thus $u'(z, t) = u''(z, t)$. Thus, the turbulent intensity is defined as follow:

$$I_x(z) = \sigma(u''(z))/\overline{U(z)}$$

with σ the standard deviation operator. It is expressed in % of $\overline{U(z)}$ at the same height and presented in Figure 6 (left). Two zones appear in the profiles. Below $z \approx H \approx 0.25$ m, the shape is representative of a wall boundary layer. Out of this layer, the turbulent intensity is low, equal to 1.5% and constant over the water column for the reference case. With waves, it strongly grows (like z^4) to reach $I_x = 5\%$ at $z = 0.9$ m , mostly thanks to the presence of the damping beach at the inlet of the working section that strongly interacts with the current and the waves and generates turbulent fluctuations.

Figure 6 (right) presents the orbital velocities of the waves, calculated by taking, at each depth z, the amplitude of $\widetilde{u}(z, t)/U_{ref}$ for U^*_{orb} and of $\widetilde{w}(z, t)/U_{ref}$ for W^*_{orb}. As expected, both orbital velocities grow towards the surface and $W^*_{orb}(z = 0) = 0$ close to the ground which prevents vertical movement. Moreover, U^*_{orb} represents 13% of $\overline{U^*}$ and W^*_{orb} represents 9% of $\overline{U^*}$ at $z = 1$ m, showing how the presence of waves at the water surface strongly impacts the whole water column.

Finally, the two cases are studied from the temporal and spectral points of view. Figure 7 (left) shows the temporal behaviour of $u^{*\prime}(t) = u'(t)/U_{ref}$ far below the water surface, at $z = 0.2$ m. For the wave case, even far from the water surface, $u^{*\prime}(t)$ is strongly marked by the wave presence as $D_e < \lambda/2$. The amplitude of its periodical fluctuations corresponds to the one announced by U^*_{orb}. For the case with current only, $u^{*\prime}(t)$ shows the classical behaviour of a low turbulent flow. Those differences are also visible looking at the Power Spectral Density of the velocity component $u^{*\prime}(t)$, shown in Figure 7 (right). The main difference between the two spectra is the energetic spike (3 orders of magnitude higher than the rest) at the wave frequency f_h. Elsewhere, they show the same classical $f^{-5/3}$ power slope (Kolmogorov 1941) and a similar level of energy.
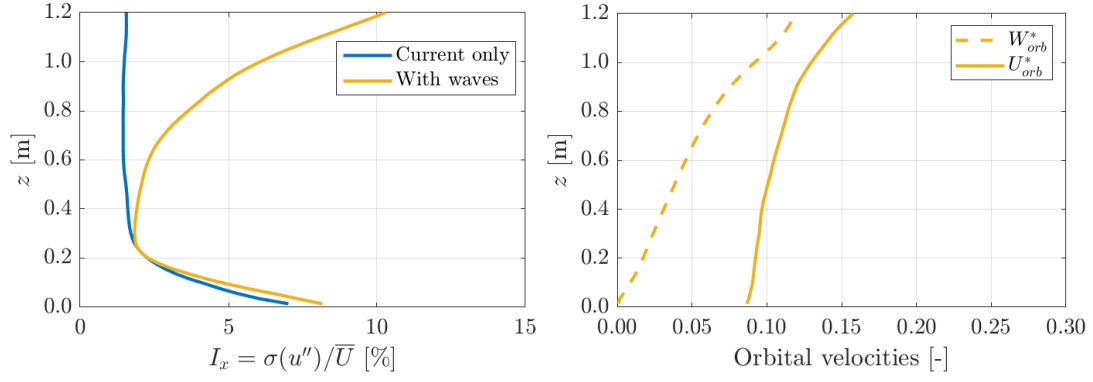
Figure 6: Left: Turbulent intensity $I_x(z)$ in the streamwise direction x at $(x, y) = (0, 0)$ m. Right: Normalised orbital-velocity in the streamwise and vertical direction at $(x, y) = (0, 0)$ m.
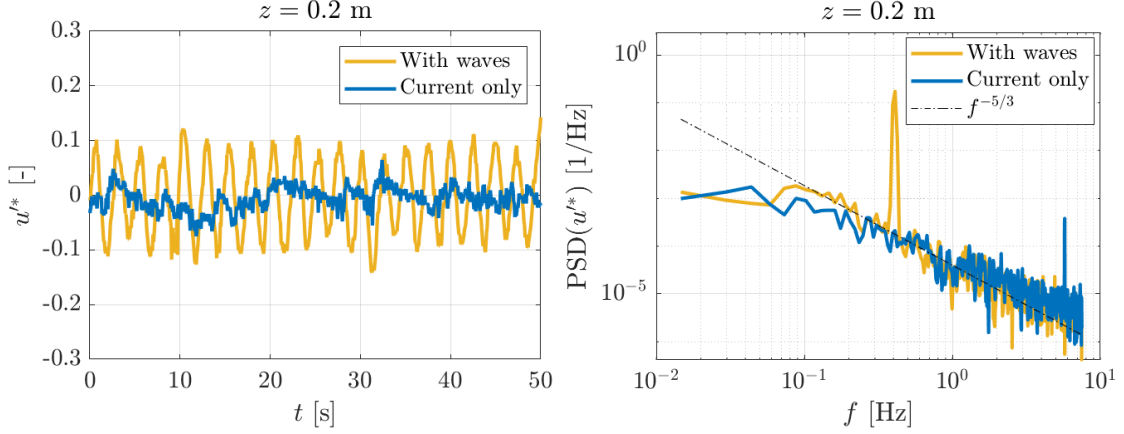

Figure 7: Temporal and spectral analysis of $u^{*\prime}$ at $z = 0.2$ m for both experimental cases.

3   Wave effects on the cylinder wake behaviour

This section aims at describing the effects of the waves on the behaviour of the cylinder wake to evaluate the main characteristics of the vortices emitted from the cylinder in the presence of waves. Several tools are used such as time average, temporal and spectral analysis of the flow fields or statistical correlation. This study is conducted in the symmetry plane of the cylinder, i.e. for $y = 0$.
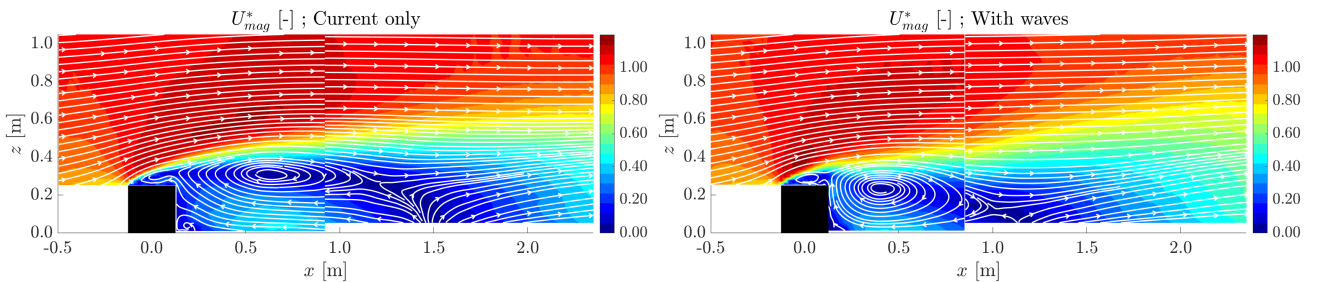
3.1   Time-averaged flow fields

Figure 8: Colormaps of the normalised velocity magnitude (U^*_{mag}) in the cylinder wake with streamlines superimposed.

Figure 8 presents the time-averaged streamlines superimposed on the velocity magnitude $U^*_{mag} = \sqrt{\overline{U^*}^2 + \overline{W^*}^2}$ in the symmetry plane of the cylinder. Figures 9 and 10 present the

time-averaged streamwise and vertical velocity maps. For the three figures, the left colormap corresponds to the current only case whereas the right colormap presents the results obtained for the wave and current case. In Figure 8, for both cases, the flow is strongly decelerated downstream of the cylinder and slightly accelerated above the cylinder. The streamlines show a strong recirculation area behind the obstacle. For both cases, a three-part structure is identified in the cylinder wake (Calhoun et al. 2001). The outer region and recirculation area are highlighted respectively by the plain line ($\overline{U^*} > 0.9$) and the dashed-line ($\overline{U^*} < 0$) in Figure 9. The sheared layer region is located in-between. Despite a common wake structure, typical of flows behind ribs in the symmetrical plane, the wakes differ between the two cases. In the presence of waves, the recirculation length is reduced by 20% while the vertical height of the wake increases by 14% at $x = 2.0$ m, meaning that the ascent rate of the wake increases with waves. The sheared region is more extended so the velocity gradients are less intense with waves than without. Moreover, waves cause a strengthening of the negative $\overline{W^*}$ area, which is also closer to the cylinder and lower in the water column, as shown in Figure 10. Furthermore, the counter-clockwise recirculation zone just behind the cylinder, at $(x, z) = (0.13 \text{ m}, 0.05 \text{ m})$, is greatly reduced with waves.

Finally, the wake recovers faster with waves: at $(x, z) = (2.0 \text{ m}, 0.25 \text{ m})$, for instance the velocity magnitude U^*_{mag} increases by 50%. In addition, at $z = 0.25$ m, the position for which $U^*_{mag} > 0.30$ is situated 0.5 m upstream for the wave case than for the current only case. This faster wake recovery might come from the growth of the sheared region and from the higher level of turbulence which dissipates the wakes, as observed for wall-mounted cube wakes (Hearst et al. 2016).
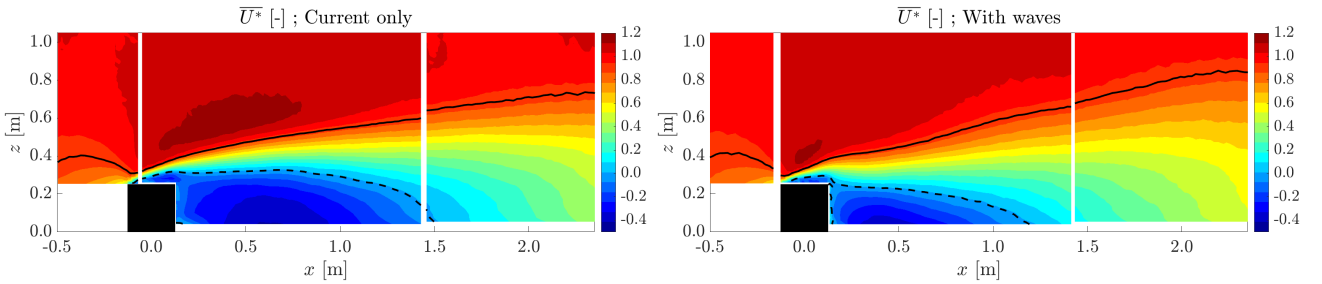

Figure 9: Colormaps of the normalised mean streamwise velocity $\overline{U^*}$ in the cylinder wake. The continuous lines correspond to $\overline{U^*} = 0.9$ and the dashed lines to $\overline{U^*} = 0$.
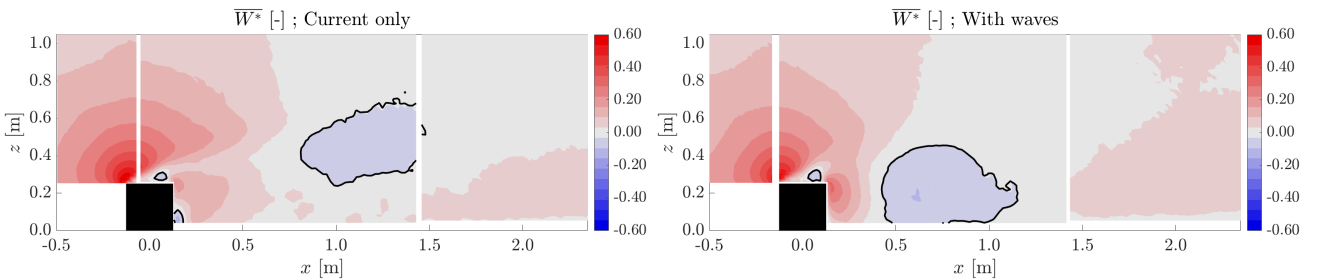

Figure 10: Colormaps of the normalised mean vertical velocity $\overline{W^*}$ in the cylinder wake. The continuous lines correspond to $\overline{W^*} = 0$.

Figures 11 and 12 present the components of the Reynolds tensor processed from the 2D PIV used in this study. The turbulent kinetic energy k_{UW} is the trace of the Reynolds tensor and $\tau_{u'w'}$ is the sheared component relative to the x and z directions. They are defined as follows:

$$k_{UW} = \frac{1}{2}(\overline{u'u'} + \overline{w'w'}) \text{ and } \tau_{u'w'} = \overline{u'w'}$$

9

Here, k_{UW} and $\tau_{u'w'}$ are normalised by U_{ref}^2 which is equivalent to use those definitions with the normalised fluctuating part of the velocity components $u^{*\prime}(t)$ and $w^{*\prime}(t)$. The normalised quantities are named k_{UW}^* and $\tau_{u'w'}^*$.

As for the mean velocity fields, k_{UW}^* and $\tau_{u'w'}^*$ are very similar for the two cases, with a high level of turbulent energy in the sheared layer. As for the mean velocity, the wake extends higher for the wave case and the average level of turbulent energy increases: at $(x, z) = (1.0 \text{ m}, 0.4 \text{ m})$, k_{UW}^* is 25% higher than without waves. The general shape of the energetic zone, highlighted by the plain-line $\tau_{u'w'}^* = -0.02$, shows furthermore some oscillations: on this iso-$\tau_{u'w'}^*$, three local maxima are noticeable at $x \approx 0.15$ m, 1.1 m and 2.0 m. This suggests an injection of energy by the waves at those specific positions in the wake. Finally, it is important to notice that, in the wave case, two high energy areas appear on the turbulent energy maps, probably linked to the three maxima of $\tau_{u'w'}^*$ previously noticed (invisible in the current only case). The higher energetic zone, named $B1$ as presented in Figure 13, is located just above the cylinder, in the region where the vortices generation mechanism happens. This points out that the vortex generation is strongly modified in the presence of waves. The second energetic area, named $B2$ in Figure 13, corresponds to the central maximum of the $\tau_{u'w'}^*$ contour and indicates that the wake is also modified by the waves during its development.
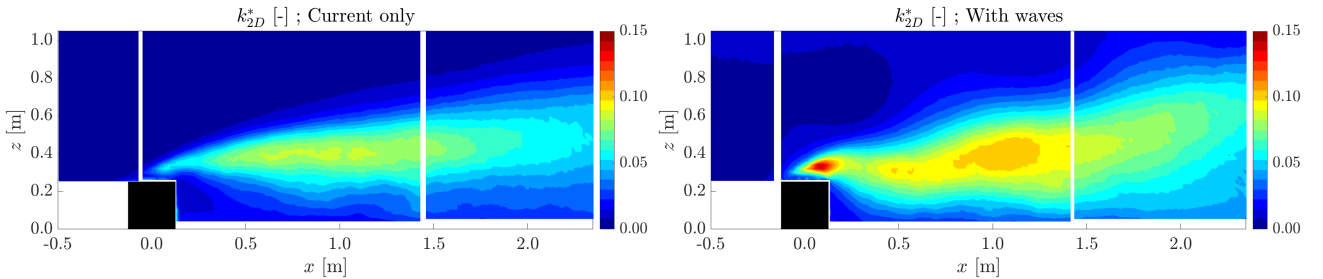

Figure 11: Colormaps of the normalised turbulent kinetic energy k_{UW}^* in the cylinder wake.
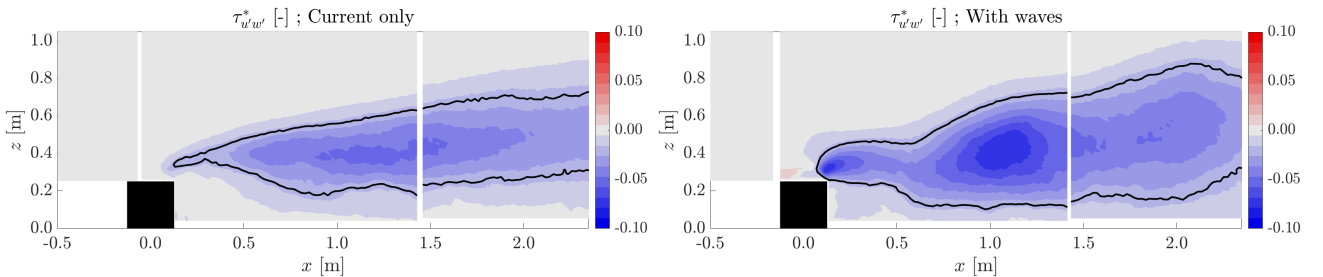

Figure 12: Colormaps of the normalised shear component of the Reynolds tensor $\tau_{u'w'}^*$ in the cylinder wake. The continuous lines correspond to $\tau_{u'w'}^* = -0.02$.

To sum up, Figure 13 presents two contours of $\tau_{u'w'}^*$ for both cases. The contour of $\tau_{u'w'}^* = -0.02$ exists in both cases and shows that the sheared layer is wider in the presence of waves than for current only. Moreover, the contour of $\tau_{u'w'}^* = -0.06$ exists for the wave case only, showing higher levels of turbulent energy with waves than without. It also highlights two specific regions where the levels of energy linked to turbulence are higher: the region $B1$, on top of the cylinder and the region $B2$, in the middle of the sheared layer. It suggests that the surface gravity waves modify the origin and the development of the cylinder wake. To complete this statistical analysis, it is important to note that the cylinder presence is impacting the whole water column, as the wave amplitude $\overline{A_{O1}}$ increases by about 20% (1.5 cm) just on top of the cylinder. Similar results have been observed in Zaman et al. (2008) and Rey et al. (2014).
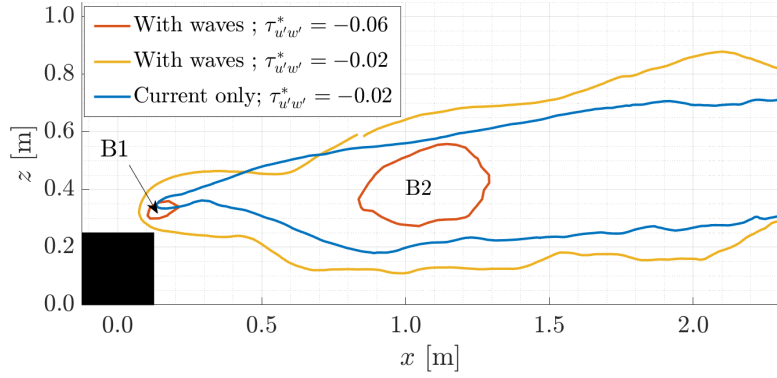
Figure 13: Schematic of the cylinder wake main features based on the Reynolds shear stress components.

3.2   Temporal and spectral analyses
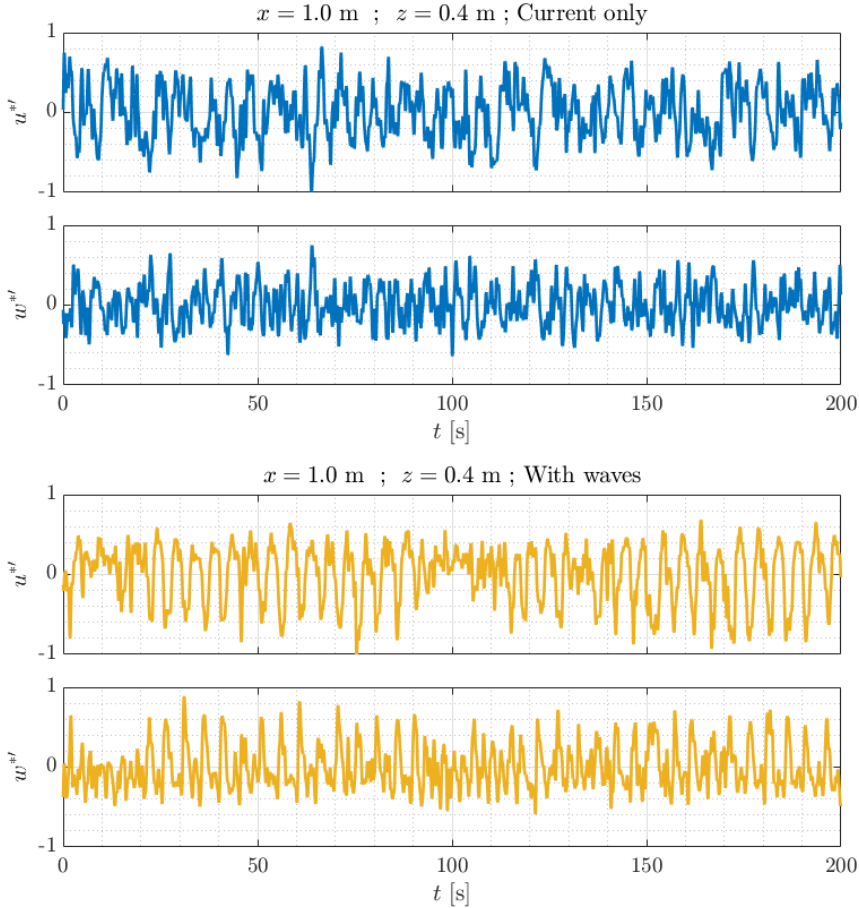

Figure 14: Normalised instantaneous fluctuating velocity components $u^{*\prime}(t)$ and $w^{*\prime}(t)$ at $(x, z) = (1.0\ \mathrm{m}, 0.4\ \mathrm{m})$, in the sheared layer. Top: Current only. Bottom: With waves.

In Figure 14, the temporal signals of $u^{*\prime}(t)$ and $w^{*\prime}(t)$ extracted in the energetic sheared layer, in $B2$ zone (cf Figure 13), are presented. For both cases and the two velocity components, the signals display strong velocity fluctuations. The fluctuations seem more regular in the wave case, repeating the same pattern every 5 s (0.2 Hz) when $t \in [20; 90]$ s or $t \in [115; 200]$ s. This frequency is close to the natural vortex shedding frequency named f_{vtx}, observed in Ikhennicheu et al. (2019). The vortex shedding frequency is defined using the Strouhal number $St = fH/U_{ref}$ as f_{vtx} depends on the incoming flow velocity U_{ref}. Here, the vortex shedding appears

11

at $St = 0.06$ (approaching the value of $St = 0.07$ presented in Ikhennicheu et al. (2019)). Thus, the vortex shedding frequency is equal to $f_{vtx} = 0.19$ Hz in the current only case and to $f_{vtx} = 0.20$ Hz in the wave case. The regular fluctuations on $u^{*\prime}(t)$ and $w^{*\prime}(t)$ signal thus does not corresponds to the wave-induced velocity fluctuations which appear at f_h (as in the wave characterisation without the cylinder, in Figure 7), but to an intensified periodic vortex shedding. On the contrary, when $t \in [0; 20]$ s or $t \in [90; 115]$ s, the velocity fluctuations are occasionally reduced compared to the current only case. The amplification of the vortex shedding phenomenon is intermittent. This may be due to the high closeness between the natural vortex shedding frequency of the cylinder f_{vtx} and half the wave frequency f_h.
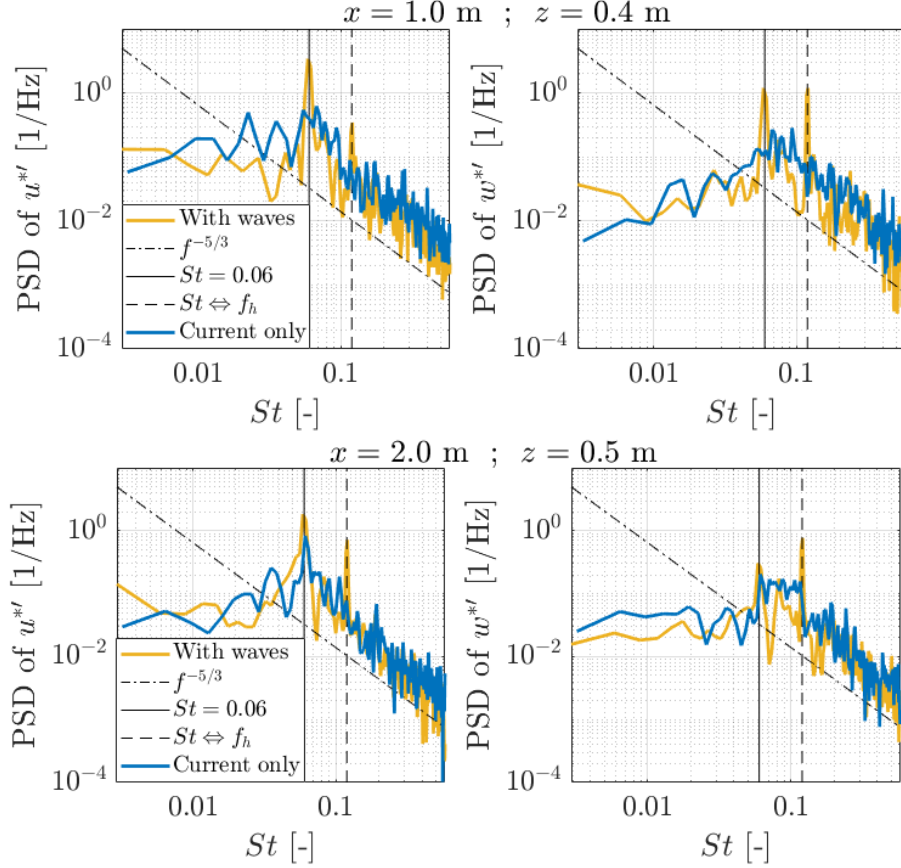

Figure 15: PSDs of the normalised velocity component $u^{*\prime}(t)$ (left row) and $w^{*\prime}(t)$ (right row) for both cases. Top: $(x, z) = (1.0 \text{ m}, 0.4 \text{ m})$ (velocity presented on the figure 14). Bottom: $(x, z) = (2.0 \text{ m}, 0.5 \text{ m})$. The Strouhal number is calculated with the reference velocity defined in the section 2.3.2: $St = fH/U_{ref}$.

To investigate the energetic frequencies of the cylinder wake, the Power Spectral Densities (PSDs) of $u^{*\prime}(t)$ and $w^{*\prime}(t)$ are plotted in Figure 15. They are calculated for both cases at two positions in the wake. The top line of the Figure presents PSDs calculated with the fluctuating velocity component extracted in $B2$ area, at $(x, z) = (1.0 \text{ m}, 0.4 \text{ m})$ (those presented in Figure 14) whereas the bottom line presents PSDs calculated 1 m downstream in the wake, at $(x, z) = (2.0 \text{ m}, 0.5 \text{ m})$, under the third local maximum observed on the $\tau^*_{u'w'}$ contour. The PSDs are plotted as function of the Strouhal number so that the peak at the vortex shedding frequency can be easily identified.

First, for the current only case, as expected, the signature of a structured vortex shedding appears at $x = 2.0$ m. It is characterised by peaks at the vortex shedding frequency f_{vtx} (thus at $St = 0.06$) on $u^{*\prime}$ (order of magnitude higher) and $w^{*\prime}$ (small peak) PSDs. At $x = 1.0$ m, on contrary, no clear spectral peak appears at f_{vtx} because the vortex shedding is not yet organised.

12

At this position, the aggregation of the vortex is in process, which explains the relatively high and constant value observed between $St = 0.05$ and $St = 0.10$ on the PSDs of $u^{*\prime}$ and $w^{*\prime}$ (Ikhennicheu et al. 2019).

Secondly, with waves, two high peaks appear on the PSDs, one at the wave frequency f_h (corresponding to a Strouhal number equal to $St = 0.12$) and the other at the vortex shedding frequency. Both peaks are visible at the two positions and for both velocity components. On the PSDs of $w^{*\prime}$, the peaks at f_h have the same or higher levels of energy than the peaks at f_{vtx}. In addition, on both PSDs of $u^{*\prime}$ and $w^{*\prime}$, the peaks at f_{vtx} are higher in the wave case than in the current case. Thereby, as there is a lot of energy available at the vortex shedding frequency, it means that the vortex are already formed and carried out by the flow. With waves, the wake organises itself quickly and has a regular and strong vortex shedding. This suggest that, with waves, no merging of the vortices is necessary to obtain a structured and energetic vortex shedding. The complex energy exchanges between the different involved frequencies are investigated in the following section.

3.3 Spatial study of the flow spectral content

To understand better the spectral content of the flow, PSDs colormaps of the normalised fluctuating streamwise and vertical velocity components are examined. As some energy exchanges occur between frequencies, this make the studied flow very complex, PSDs are calculated over all PIV plane height at five fixed x-positions, as done in Magnier et al. (2021). Figures 16 and 17 respectively present the obtained PSD maps of $u^{*\prime}(t)$ and $w^{*\prime}(t)$, expressed as a function of the Strouhal number $St = fH/U_{ref}$, for both cases.
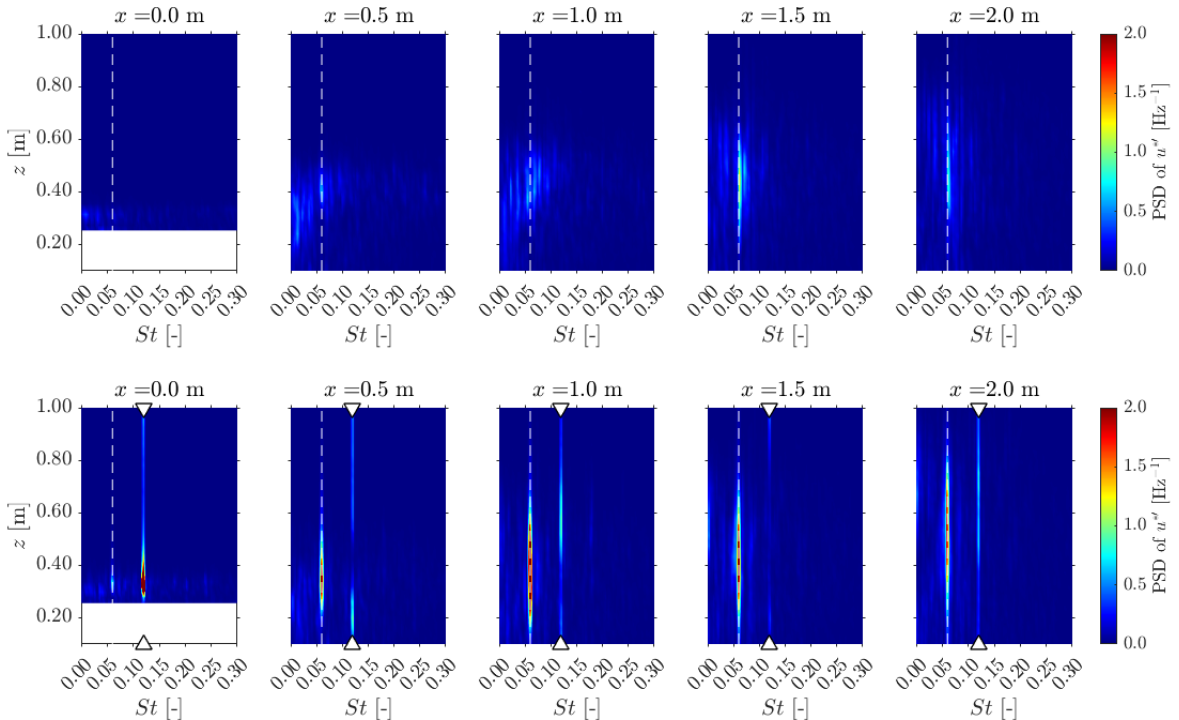

Figure 16: Colormaps of the PSDs of $u^{*\prime}$ at 5 x-positions in the cylinder wake. The x-coordinate is indicated on top of each (St, z) map. Top: Current only. Bottom: With waves. Dashed lines correspond to f_{vtx} and the white arrows on top and bottom of each map correspond to f_h. The colour scale is fixed to see the majority of the content which is present between 0.0 and 2.0, thus maxima are cut in the wave case.
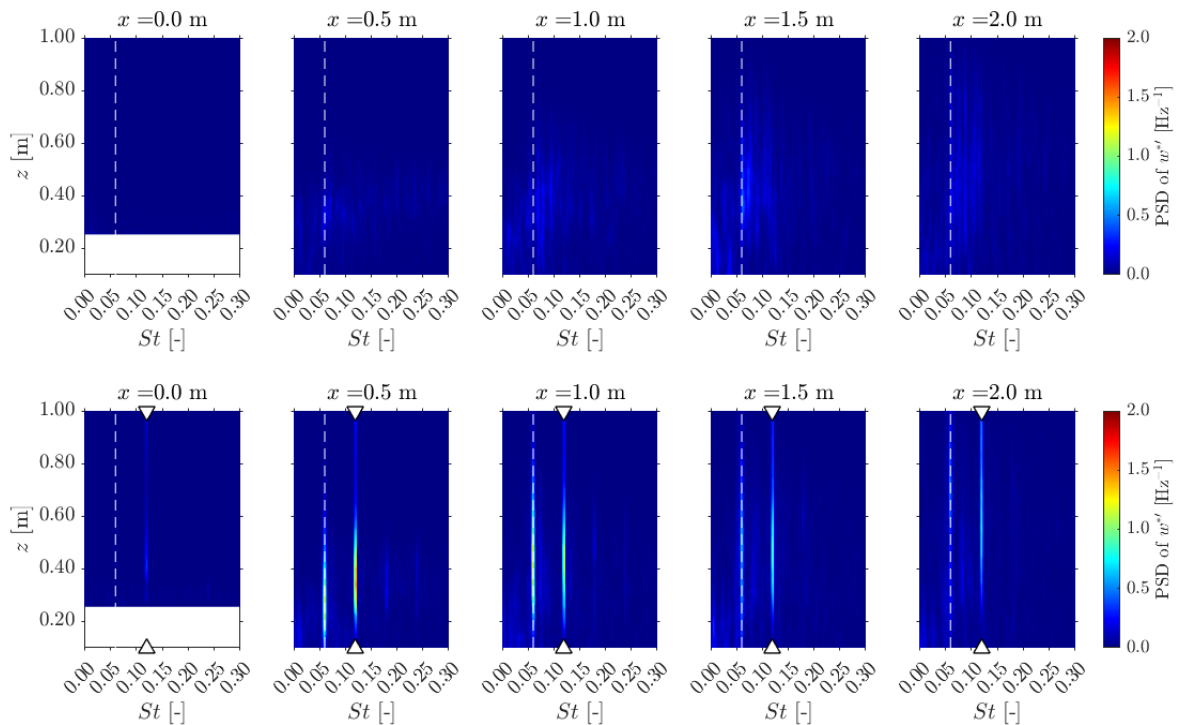
Figure 17: Colormaps of the PSDs of $w^{*\prime}$ at 5 x-positions in the cylinder wake. The x-coordinate is indicated on top of each map. Top: Current only. Bottom: With waves. Dashed lines correspond to f_{vtx} and the white arrows on top and bottom of each map correspond to f_h.

On one hand, in the current only case, on PSD of $u^{*\prime}$, a clear and distinct peak at f_{vtx} appears in the sheared layer from $x = 1.5$ m. Its level of energy reaches a maximum of 1.0 at $(x, z) = (1.5\,\mathrm{m}, 0.4\,\mathrm{m})$, in the region where Reynolds tensor terms are maximum without waves. Moreover, the peak moves slightly toward the surface as z increases, staying in the highest turbulent kinetic energy zone (Figure 11). No well-shaped and energetic peak emerges in the PSDs of $w^{*\prime}$. As described by Ikhennicheu et al. (2019), Mercier et al. (2020) and Magnier et al. (2021), the vortex shedding organises itself as the distance to the obstacle increases, becoming more and more regular and energetic. It happens when the flow becomes 2D in the central part of the cylinder (Martinuzzi et al. 1993).

On the other hand, in the wave case, the PSD maps are much more complex. On top of the cylinder ($x = 0$), the signature of the waves is visible at the wave frequency f_h for both velocity components. For the PSDs of $w^{*\prime}$ (at x=0), the energy of the peak at f_h is low (<0.5) and rather homogeneous along z. For the PSDs of $u^{*\prime}$ at $x = 0$, the energy available at f_h decreases when the depth increases (such as the orbital velocities) until $z = 0.5$ m. Below, the energy level increases notably to reach its absolute maximum (of all PSDs colormaps) at $x = 0.32$ m. The absolute maximum is equal to 5.9 (out of colour scale). That strong increase, just above the cylinder, of the energy available at f_h, suggests the generation of eddies from the interaction of the wave-induced motion with the cylinder (Ting et al. 1994). Moreover, this high energy peak appears exactly in the $B1$ region. The high turbulent energy levels observed in that region are thus coming from the eddies resulting from the cylinder-wave-current interaction. That phenomenon is not visible on the PSD of $w^{*\prime}$.

Downstream from the cylinder, the two same frequencies stand out thanks to their high energy levels : f_h and f_{vtx}. Their energy levels strongly vary depending on x and z positions. For the $w^{*\prime}$ PSD maps, the peaks at f_h and f_{vtx} appear at the same depth and the one linked to the vortex shedding only is slightly less energetic. In addition, peaks of smaller amplitude appear at the harmonics $3f_{vtx}$ and $4f_{vtx}$. They are visible at the depth of the f_h peak, when its

14

energy is high enough (> 1.0). On the contrary, in $u^{*\prime}$ PSD maps, the energy levels of the peak at f_h seem to be strongly reduced by the presence, at the same position x and z, of a peak at f_{vtx}, i.e in the sheared layer. As observed in Figure 15, the peak corresponding to the vortex shedding phenomenon is different with waves than without. With waves, the f_{vtx} peak is present from $x = 0.5$ m. At $x = 1.5$ m (the position of the highest peak for the current only case), its energy ($= 2.4$) is two times higher than without waves. Before $x = 1.0$ m, no significant peak appears in the current only case whereas it is the case with waves with the highest energy peaks. In the cylinder wake, the highest peak is found at $x = 1.0$ m and $z = 0.4$ m whereas the level of energy reaches 3.4, three times higher than the maximum observed for the current only case. The peaks at f_h and f_{vtx} are the signature of the high-energy vortex structures, which develop from the top face and top corners of the cylinder, and then become larger when the distance to the obstacle increases. More precisely, those PSD maps suggest the generation of eddies at f_h in the $B1$ region. The energy is then transferred to f_{vtx} when one of the two eddy is shed and carried away by the flow. The closeness between $2f_h$ and f_{vtx} should help this energy feeding on top of the cylinder and transfering between frequencies in the near wake.

3.4 Length scale of the coherent structures

This sub-section presents a statistical estimation of the vortex size, as done in Magnier et al. (2021). To do this, the two-point spatial correlation coefficient of both the streamwise and the vertical velocity components is calculated. This coefficient is defined as follows:

$$R_{v_i v_i}(x_{ref}, z_{ref}, x, z) = \frac{\overline{v_i'(x_{ref}, z_{ref})v_i'(x, z)}}{\sqrt{\overline{v_i'^2(x_{ref}, z_{ref})}}\sqrt{\overline{v_i'^2(x, z)}}}$$

where v_i is the fluctuating velocity component chosen (u or w), to which is added a random number between 0 and 1. The coordinates (x_{ref}, z_{ref}) are those of a fixed reference point. This fixed reference point is chosen alternatively along three vertical lines at $x = 0.5$ m, 1.0 m and 2.0 m. Each vertical line is composed of 15 points, corresponding to the symbols (triangles or stars) in Figure 18. When $R_{v_i v_i}(x_{ref}, z_{ref}, x, z)$ is plotted as a function of x and z, for a given reference pair (x_{ref}, z_{ref}), a correlation colormap with values between -1 and 1 (not shown here) is obtained, as presented in Magnier et al. (2021). $R_{v_i v_i}$ is equal to 1 at the reference point because it is correlated to itself. As x and z vary from the reference point, the value of $R_{v_i v_i}$ decreases. Connecting all the positions for which $R_{v_i v_i} = 0.4$, an ellipse is obtained. We can therefore hypothesize that velocity vectors are closely related to each other when the correlation level is higher than 0.4. Thus, it is considered than when $R_{v_i v_i} > 0.4$, the statistical link between the vectors is strong. Estimating the size of this zone enables an assessment of a statistical length scale related to the size of the coherent vortices.

The estimation of the size of the zone where $R_{uu} > 0.4$ or $R_{ww} > 0.4$ is done in x and z directions, which gives four estimators of the statistical length scale of the vortices. They are named $L_{v_i j}$, where v_i is the direction of the fluctuating velocity used (u or w, as in the definition of the correlation coefficient) and j is the axis along which the size of the area $R_{v_i v_i} > 0.4$ is estimated (x or z). The size $L_{v_i j}$ has no dimension because it depends on the correlation threshold chosen, here 0.4. Figure 18 presents those four length scales. The top line of the figure presents L_{ux} and L_{uz} profiles at $x = 0.5$ m, 1.0 m or 2.0 m. The bottom line presents L_{wx} and L_{wz} profiles at the same x-positions.

For both cases, as expected, one finds $L_{v_i j} = 0$ in the uniform flow, out of the sheared layer. Thus, detected eddies are linked to the cylinder wake. This confirms furthermore that the wave-induced periodical motion does not affect the calculation of these scales which are equal to zero outside the wake of the cylinder, where orbital velocities are well-marked. At first glance, for the wave case, the length scales are always larger than the ones observed for the

current only case. In fact, excepted for L_{ux} and L_{uz} at $x = 0.5$ m in the centre of the sheared layer ($z \approx 0.4$ m) and for L_{wx} and L_{wz} at $x = 2.0$ m in the bottom part of the water column ($z < 0.5$ m), the statistical length scales are at least twice bigger with the waves than without. Moreover, the length scales reach their maximum value higher in the water column with waves than without, as it happens to be located in the sheared layer which has a stronger ascent rate, as observed in Figure 9.

Therefore, the presence of waves at the surface of the water also affects the size of the vortices generated by the cylinder. The waves inject energy around the cylinder, where the vortices are generated. Thus, the energy of the vortices is higher and their rotation is more intense, resulting in a larger area of influence of those structures.
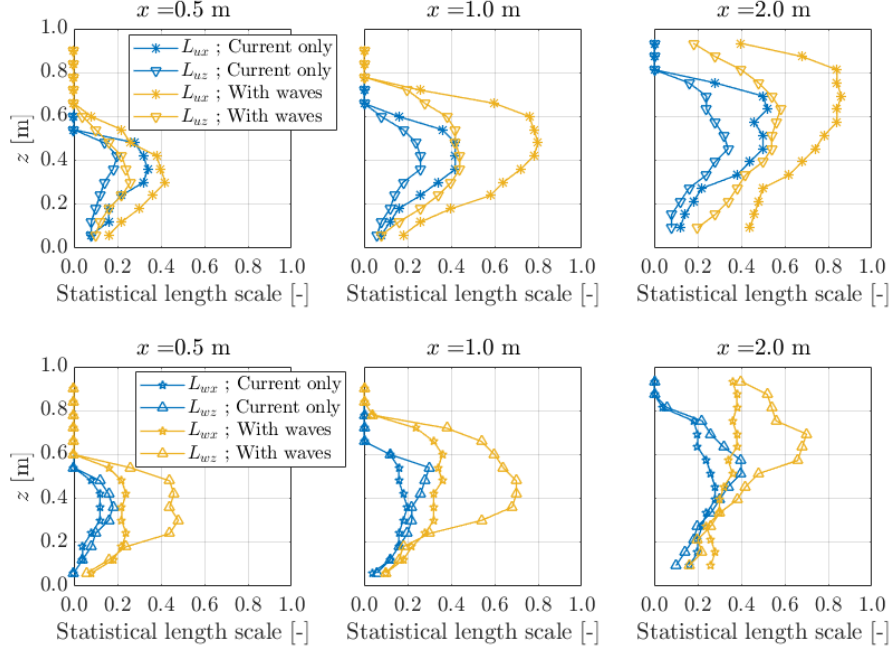

Figure 18: Statistical size of the coherent structures in the streamwise and vertical direction.

3.5 Distribution of the preferential zones of waves effects

To complete the observations previously done from the PSD maps (Figure 16) about disappearance of f_h in the sheared layer, another tool is used. It aims at highlighting the areas of the flow which contain the wave frequency f_h, and are synchronised to the free surface. To do so, the cross-correlation coefficient is calculated between the elevation of the free surface just above the cylinder centre $(x, y) = (0, 0)$ named $\eta_A(t)$ and the velocity component $u'(t)$ at every position (x, z) of the PIV planes:

$$R_{u\eta_A}(x, z, t) = \frac{\overline{u'(x, z, t)\eta_A(t)}}{\sqrt{\overline{u'^2(x, z, t)}}\sqrt{\overline{\eta_A^2(t)}}}$$

Then, for each position (x, z), the maximum correlation coefficient $R_{u\eta_A}^{\max}(x, z) = \max\left(R_{u\eta_A}(x, z, t)\right)$ is kept and plotted as a colormap in Figure 19. To help the figure reading, positions where the statistical link is not strong enough $(R_{u\eta_A}^{\max}(x, z) < 0.4)$ appear in white. So, every coloured position of the Figure 19 map corresponds to a point showing a significant response to the wave frequency.

This map highlights two regions in the flow captured by PIV measurements. The first one is roughly the sheared layer, which is not correlated to wave frequency, i.e. $R_{u\eta_A}^{\max} < 0.4$.
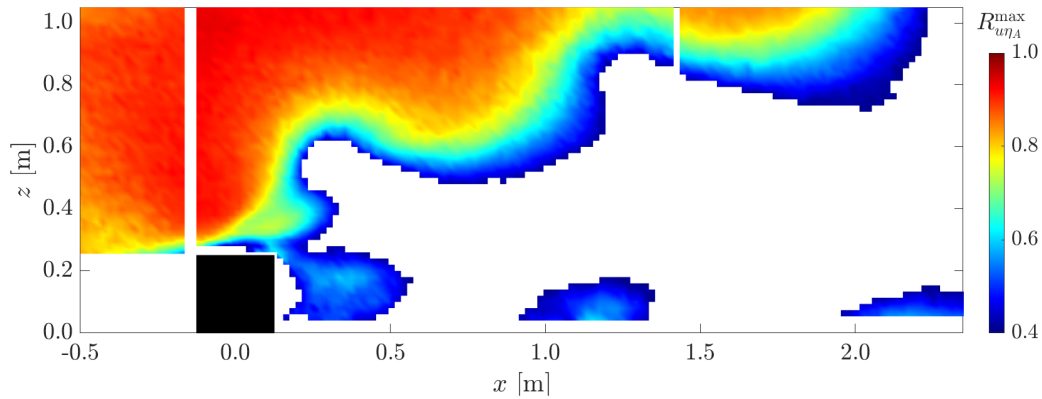
16

Figure 19: Colormap of the maximum of the correlation coefficient $R_{u\eta_A}^{\max}(x,z)$ [-] between $\eta_A(t)$ and $u'(x,z,t)$. White areas correspond to interstices between PIV measurement planes or positions where $R_{u\eta_A}^{\max}(x,z) < 0.4$.

On the contrary, outside the wake, the maximum level of correlation is high (for example, $R_{u\eta_A}^{\max}(0.5\text{ m}, 1.0\text{ m}) = 0.91$), and increases as the distance normal to the wake limit increases. However, the shape of the region not correlated to η_A (in which f_h is not significantly present) is more complex than the envelope of the sheared and energetic layer, materialised by $\tau_{u^{*\prime}w^{*\prime}} = -0.02$ in Figure 12.

Two lobes, centred around $(x,z) = (0.3\text{ m}, 0.5\text{ m})$ and $(x,z) = (1.3\text{ m}, 0.7\text{ m})$, display no correlation to $\eta_A(t)$. They are, however, located in the outer region, outside of the sheared layer. This is in agreement with Figure 16 where almost no energy is associated with f_h at $x = 1.5$ m. In addition, between those two areas with low correlation level, the wave-induced periodical fluctuations seem to persist in the cylinder wake, not being cancelled by the large velocity fluctuations caused by the vortices. These two positions ($x \approx 1.1$ m and $x \approx 2.0$) correspond to the x-positions of the two local maxima (on top of $B2$ area and the one downstream) of the curve $\tau_{u^{*\prime}w^{*\prime}} = -0.02$ in Figure 13. Those two regions seem to be favoured places for the waves to act on the development of the wake. Combined with the energy at f_{vtx}, it explains the high value of k_{UW}^* and $\tau_{u'w'}^*$. Moreover, around the cylinder, the flow is well correlated to the free surface dynamic (η_A). That is in agreement to PSD of $u^{*\prime}$ results (Figure 16) and confirms that in the region where the vortex generation occurs, the flow is phased to the free surface periodical variations at f_h. Thereby, vortices are generated at the wave frequency directly by the wave-induced motion and the mean flow carries one of two vortices downstream.

3.6 Vortex generation and development with waves

This section aims to understand the mechanisms underlying the strong modification of the cylinder wake due to the waves. To do so, the velocity fields are averaged at the wave frequency and at the vortex shedding frequency to analyse how the wave-induced motion acts on the vortex generation and wake development. In the phase average figures shown below, only one vector out of two is plotted to make them easier to read.

Figure 20 presents the phase average of the flow at the wave frequency, for five phases, every $\pi/2$. The phase is defined as t/T_h with $T_h = 1/f_h$ the wave period. The phase is set to zero when a wave trough is passing on top of the cylinder. At this phase, the wave-induced motion is in the same direction than the current. Thus, on top of the cylinder ($x = 0$), when $t/T_h = 0$, the current is maximum in x-direction. On those phase-averaged velocity fields, vortices are visible near the cylinder, under about $z = 0.5$ m at $x = 0$. After $x = 1.0$ m, the vortices disappear. That is in agreement with the PSD results, presented in the Figure 16, which show that there is energy at f_h only near the cylinder. It also confirms the hypothesis that, at $x = 0$,
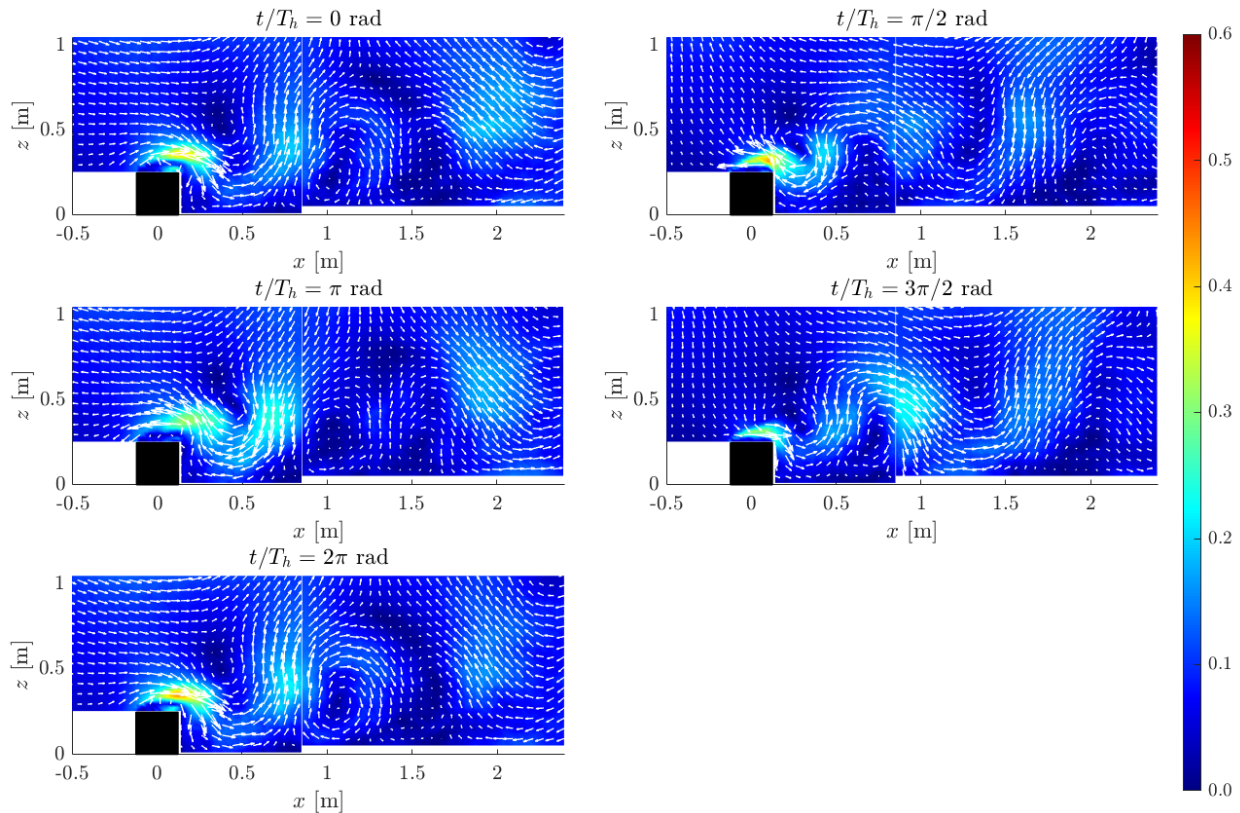
Figure 20: Phase average of the velocity fields at the wave frequency f_h, in the wave case. In the background, colormaps of the magnitude of the fluctuating velocity $u_{mag}^{*\prime}$. In the foreground, vectors of the velocity fluctuating fields.

the reinforcement of the energy at f_h near the cylinder is linked to vortex generation by the wave induced-motion (Ting et al. 1994).

Then, the phase average of the flow at the vortex shedding frequency is presented in Figure 21 for nine phases every $\pi/4$. The phase is defined as t/T_{vtx} in radian, with $T_{vtx} = 1/f_{vtx}$ the vortex shedding period. As $f_{vtx} \approx \frac{1}{2}f_h$, the phase is set to be equal to zero ($t/T_{vtx} = 0$) when a wave trough is on top of the cylinder. Thus, as $T_{vtx} \approx 2T_h$ and the waves are regular and linear, a wave trough is also on top of the cylinder when $t/T_{vtx} = \pi$ and $t/T_{vtx} = 2\pi$ whereas a wave crest is on top of the cylinder when $t/T_{vtx} = \pi/2$ and $t/T_{vtx} = 3\pi/2$. Moreover, as expected, the flow phase averages are identical when $t/T_{vtx} = 0$ and 2π.

In the figure, vortices clearly appear at each phase. Several methods exist to determine the centre of the vortices as Zhou et al. (1999) or Graftieaux et al. (2001). The vortex centre detection method previously developed by Graftieaux et al. (2001) has been adapted in Druault et al. (2016) and Ikhennicheu et al. (2019) for PIV data as the one used in this article. The vortex cores identified by this method satisfy the following properties: its neighbouring phase averaged velocities have to be oriented in the same direction and must have a higher absolute value than the centre velocity which has to be very slow. They mainly correspond to vortex core identifiable by sight. In the present work the vortex core position is used to illustrate the wave effects on the cylinder wake and no calculation has been made from it, so the precision of the positioning does not lead to any particular bias in the study. Thus, the vortex cores have only been identified by sight and have to fulfil criteria mentioned above. The wider vortex appears when $t/T_{vtx} = 2\pi$ rad (named V_A). Its core is marked by a red dot and is circled with arrows showing that it rotates clockwise. Its maximum velocity magnitude is equal to $u_{mag}^{*\prime} = \sqrt{u^{*\prime 2} + w^{*\prime 2}} = 0.40$ and its core is high in the water column: $(x, z) = (2.3 \text{ m}, 1.0 \text{ m})$. As the vortex V_A is visible here, it means that it appears every T_{vtx}. The vortex V_A is created
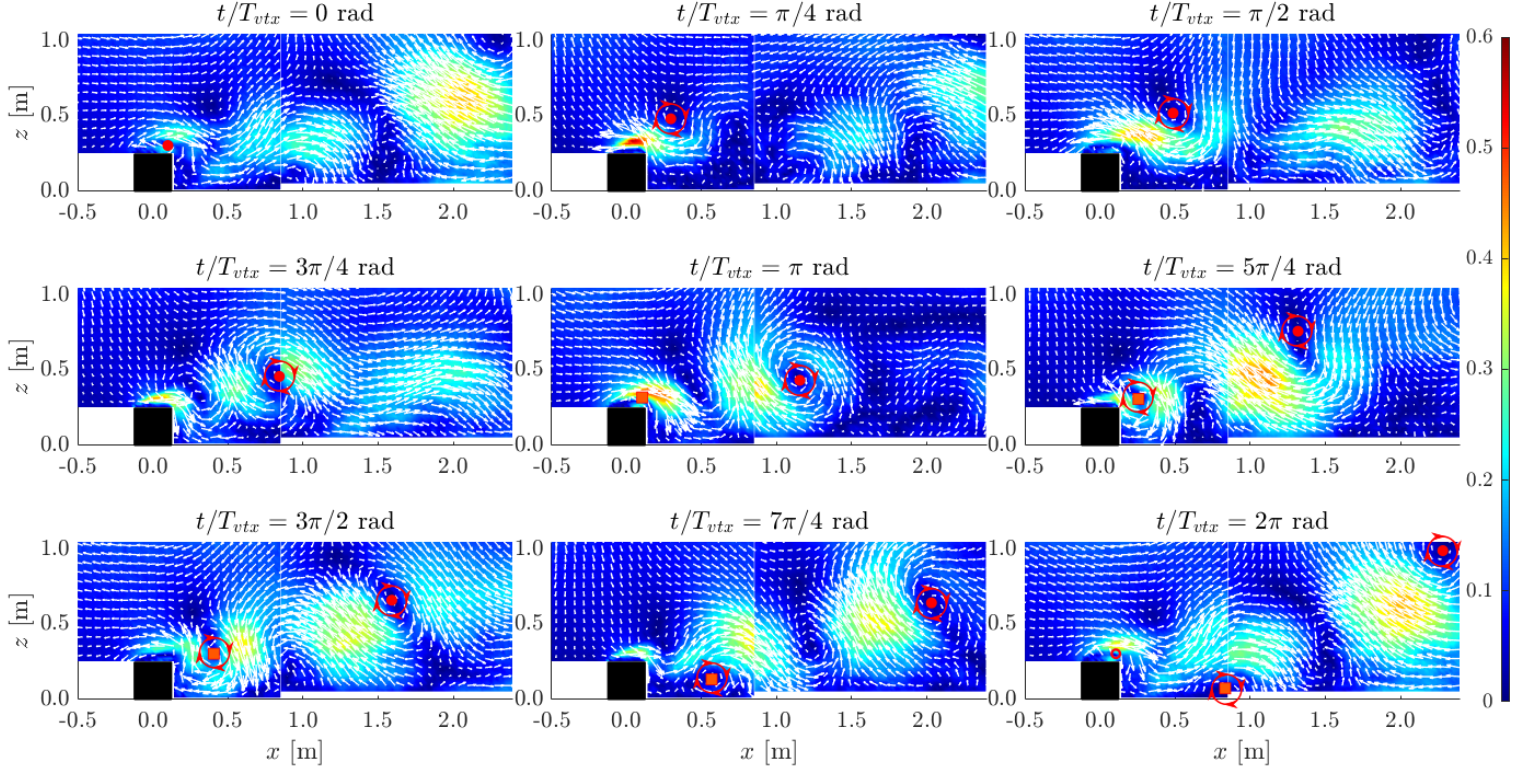
Figure 21: Phase average of the velocity fields at the vortex shedding frequency f_{vtx}, in the wave case. In the background, colormaps of the magnitude of the fluctuating velocity $u^{*\prime}_{mag}$. In the foreground, vectors of the velocity fluctuating fields. The symbols (red full dot, orange square, red empty dot) mark the core of the vortices, from their birth to their exit of the PIV planes. They are circled with arrows giving the rotating direction

above the cylinder when $t/T_{vtx} = 0$ rad, in $B1$ area, where the k^*_{UW} level is maximum on top of the cylinder (defined in Figure 13). When $t/T_{vtx} = \pi/4$ rad, the young vortex is responsible for a high velocity area ($u^{*\prime}_{mag} = 0.57$ m/s) in $B1$ region too. Then, the vortex V_A moves in the sheared layer direction, while intensifying. When moving downstream, carried by the flow, the vortex is lifted three times upward by the wave-induced motion: between 0 and $\pi/4$, between π and $5\pi/4$, and between $7\pi/4$ and 2π, as shown in Figure 22. This happens when the rising front of the wave (from trough to crest), responsible for strong orbital velocities toward z, passes on top of the cylinder. It occurs more than twice in 2π because the vortex moves downstream, opposing wave direction. Moreover, no merging of V_A with other eddies is observed in the symmetry plane studied here.

The vortex V_A is followed by a smaller vortex (named V_C and marked by the orange square), which stays near the tank bed and rotates clockwise, in the same direction as V_A. However, each time the vortex V_A is lift by the wave-induced motions, the vortex V_C is pushed towards the bottom ($-z$), and stays small and weak. In fact, a vortex rotating clockwise is generated two times during a vortex shedding period T_{vtx}, thus at the wave frequency f_h. Only one of those two vortices is shed in the cylinder wake. The selection of one of two vortices should be a combination of the favoured vortex shedding frequency of the cylinder wake and the wave-induced motion which pulls every second vortex upwards.

Finally, Figure 22 displays the contour of $R^{\max}_{u\eta_A}$ to highlight the places where wave-induced velocity fluctuations are present. The positions of the core of the clockwise vortices (V_A and V_C) are extracted from the phased-average (Figure 21) and are superimposed on the contour
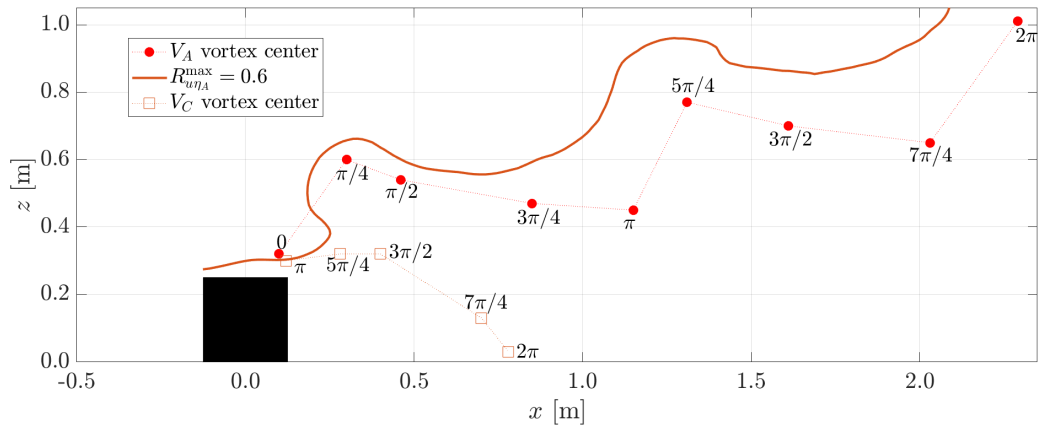
Figure 22: Contour $R_{u\eta_A}^{\max}$ in the wave case. The trajectories of the two clockwise vortex cores are plotted for a vortex shedding period. The phases corresponding to the cores' positions are indicated near the markers.

of $R_{u\eta_A}^{\max}$. Near each vortex core marker, the corresponding phase is indicated. In this Figure, the first thing that stands out is the concordance between the lobes of $R_{u\eta_A}^{\max}$ and the trajectory of the V_A vortex. The lobes appear when vortex V_A is pulled up by the wave-induced motion. Elsewhere, V_A core trajectory is rather horizontal (slightly oriented downwards) and the height of $R_{u\eta_A}^{\max}$ contour slightly decreases. Thus, those regions which are not correlated with the waves periodical fluctuations are mainly related to the intense vortex V_A. As observed thanks to the phase averages, one can see that even if V_A and V_C are generated at the same place, they do not have the same trajectory and therefore the same development. One is transported into the sheared layer while the other disappears, pressed against the floor by the orbital velocities. This is due to the combined action of the waves which changes the nature of the vortex generation and then strengthens the vortex by pulling it upwards regularly. The trajectory of the vortex favoured by the waves is thus a staircase, contrary to what was observed by Ikhennicheu et al. (2019) without waves.

4   Conclusion

This article presents an experimental study of the effects of waves propagating against the current on the wake and the vortex shedding induced by a bottom mounted square cylinder, set perpendicular to the flow. The study parameters are chosen to be representative of high potential tidal energy sites in the English Channel.

The flow conditions are first characterised without the obstacle and compared to in-situ references. Two cases are studied. The current only case is the reference one (corresponding to calm weather condition), in which the cylinder wake has been studied previously and its vortex shedding characterised. The wave case (average peak period and wavelength, severe significant wave height) is compared to the current only case to understand how the presence of waves modifies the cylinder wake and the vortex shedding.

Thanks to the time average velocities, the turbulent kinetic energy and the Reynold shear stress, it is established that, in this wave case, the three-part structure of the cylinder wake is globally conserved. However, the recirculation length decreases by 20% whereas, $8H$ downstream the obstacle, the wake vertical height increases by 14%. The level of turbulent energy increases by 25% in the middle of the sheared layer with a modified distribution. The absolute maxima of turbulent kinetic energy and Reynolds shear stress appear on top of the cylinder, instead of in the middle of the sheared layer, demonstrating that waves modify the vortex generation. The spectral and statistical analyses show a strong increase of the energy at the

wave frequency around the cylinder. In fact, the vortices are generated around the cylinder at the wave frequency. Downstream, the energy is transferred to the vortex shedding frequency, corresponding to a Strouhal number equal to 0.06. Thus, the energy at the vortex shedding frequency increases by one order of magnitude in the middle of the shear layer. The energy transfer between the wave and the vortex shedding frequency is the result of the combination of two phenomena. On one hand, the favoured vortex shedding frequency is twice the wave frequency. On the other hand, the wave-induced motion causes the ascent of one of the two vortices emitted at the wave frequency, whereas the other one is pushed deeper at every wave, as shown by the phase averages. Thus, the waves, acting on the vortex generation and the wake development, cause a doubling in the size of the vortices.

The wave case chosen in this study, for its representativeness of high potential tidal energy sites, has the particularity of having a wave frequency twice the vortex shedding frequency. The energy transfers which occur between the vortex shedding frequency and the wave frequency seem to be particularly ruled by this factor and highlight the need to study the wave frequency effect on the cylinder wake. Moreover, the current investigation is limited to the median plan of the obstacle whereas the flow generated is three-dimensional. The conclusions drawn on the wave effect on the cylinder wake have to be confirmed outside of the median plane of the cylinder. Finally, the effect of the direction of propagation of the waves, relative to the current, has to be investigated too.

References

Barman, K., K. Debnath, and B. S. Mazumder (2016). "Turbulence between two inline hemispherical obstacles under wave-current interactions". In: *Advances in Water Resources* 88, pp. 32–52. DOI: 10.1016/j.advwatres.2015.12.001.

Bennis, A. C., L. Furgerot, P. Bailly du Bois, E. Poizot, Y. Méar, and F. Dumas (2022). "A winter storm in Alderney Race: Impacts of 3D wave–current interactions on the hydrodynamic and tidal stream energy". In: *Applied Ocean Research* 120, p. 103009. DOI: 10.1016/j.apor.2021.103009.

Bougis, J. (1993). *Les houles périodiques simples*. Tech. rep. Université de Toulon et du Var. URL: https://www.scs-ingenierie.com/pdf/cours/Houles.pdf.

Calhoun, R. J. and R. L. Street (2001). "Turbulent flow over a wavy surface: Neutral case". In: *Journal of Geophysical Research: Oceans* 106.C5, pp. 9277–9293. DOI: 10.1029/2000jc900133.

Chen, Y. L., J. B. Hung, S. L. Hsu, S. C. Hsiao, and Y. C. Wu (2014). "Interaction of water waves and a submerged parabolic obstacle in the presence of a following uniform/shear current using RANS model". In: *Mathematical Problems in Engineering* 2014. DOI: 10.1155/2014/896723.

Druault, P. and G. Germain (2016). "Analysis of hydrodynamics of a moving trawl codend and its fluttering motions in flume tank". In: *European Journal of Mechanics, B/Fluids* 60, pp. 219–229. DOI: 10.1016/j.euromechflu.2016.06.010.

Filipot, J.-F., M. Prevosto, C. Maisondieu, M. Le Boulluec, and J. Thomson (2015). "Wave and turbulence measurements at a tidal energy site". In: *IEEE/OES Current, Waves and Turbulence Measurement (CWTM)*. DOI: 10.1109/CWTM.2015.7098128.

Furgerot, L., A. Sentchev, P. Bailly du Bois, G. Lopez, M. Morillon, E. Poizot, Y. Méar, and A. C. Bennis (2020). "One year of measurements in Alderney Race: preliminary results from database analysis". In: *Phil. Trans. R. Soc A* 378, p. 20190625. DOI: 10.1098/rsta.2019.0625.

Gaurier, B., T. Bacchetti, J.-V. Facq, and G. Germain (2010). *Essais combinés houle-courant. Caractérisation des conditions générées au bassin de Boulogne-sur-Mer*. Tech. rep.

Graftieaux, L., M. Michard, and G. Nathalie (2001). "Combining PIV, POD and vortex iden- tification algorithms for the study of unsteady turbulent swirling flows". In: *Measurement Science and Technology* 12.9, pp. 1422–1429. DOI: 10.1088/0957-0233/12/9/307.

Hearst, R. J., G. Gomit, and B. Ganapathisubramani (2016). "Effect of turbulence on the wake of a wall-mounted cube". In: *Journal of Fluid Mechanics* 804, pp. 513–530. DOI: 10.1017/jfm.2016.565.

Ikhennicheu, M., G. Germain, P. Druault, and B. Gaurier (2019). "Experimental study of co- herent flow structures past a wall-mounted square cylinder". In: *Ocean Engineering journal* 182, pp. 137–146. DOI: 10.1016/j.oceaneng.2019.04.043.

Kemp, P. H. and R. R. Simons (1981). "The interaction between waves and a turbulent current : waves propagating with the current". In: *Journal of Fluid Mechanics* 116, pp. 227–250. DOI: 10.1017/S0022112082000445.

Kolmogorov, A. N. (1941). "The Local Structure of Turbulence in Incompressible Viscous Fluid for Very Large Reynolds Numbers". In: 434.1890, pp. 9–13. URL: https://about.jstor.org/terms.

Magnier, M., P. Druault, and G. Germain (2021). "Experimental investigation of upstream cube effects on the wake of a wall-mounted cylinder: Wake rising reduction, TKE budget and flow organization". In: *European Journal of Mechanics, B/Fluids* 87, pp. 92–102. DOI: 10.1016/j.euromechflu.2021.01.004.

Magnier, M., B. Gaurier, G. Germain, and P. Druault (2022). "Analysis of the wake of a wide bottom-mounted obstacle in presence of surface wave following tidal current". In: *Trends in Renewable Energies Offshore*, pp. 151–159. DOI: 10.1201/9781003360773-18.

Martinuzzi, R. J. and C. Tropea (1993). "The flow around surface-mounted, prismatic obstacles placed in a fully developed channel flow". In: *Journal of Fluids Engineering, Transactions of the ASME*. DOI: 10.1115/1.2910118.

Mercier, P., M. Ikhennicheu, S. Guillou, G. Germain, E. Poizot, M. Grondeau, J. Thiébot, and P. Druault (2020). "The merging of Kelvin–Helmholtz vortices into large coherent flow structures in a high Reynolds number flow past a wall-mounted square cylinder". In: *Ocean Engineering* 204, p. 107274. DOI: 10.1016/j.oceaneng.2020.107274.

Moreau, M., G. Germain, G. Maurice, and A. Richard (2022). "Sea states influence on the behaviour of a bottom mounted full-scale twin vertical axis tidal turbine". In: *Ocean Engi- neering* 265, p. 112582. DOI: 10.1016/j.oceaneng.2022.112582.

Perez, L., R. Cossu, A. Grinham, and I. Penesis (2020). "Evaluation of wave-turbulence de- composition methods applied to experimental wave and grid-generated turbulence data". In: *Ocean Engineering* 218, p. 108186. DOI: 10.1016/j.oceaneng.2020.108186.

Rey, V., J. Charland, and J. Touboul (2014). "Wave-current interaction in the presence of a three-dimensional bathymetry: Deep water wave focusing in opposing current conditions". In: *Physics of Fluids* 26.9. DOI: 10.1063/1.4894740.

Roy, S., K. Debnath, and B. S. Mazumder (2017). "Distribution of eddy scales for wave current combined flow". In: *Applied Ocean Research* 63, pp. 170–183. DOI: 10.1016/j.apor.2017.01.005.

Roy, S., S. S. Samantaray, and K. Debnath (2018). "Study of turbulent eddies for wave against current". In: *Ocean Engineering* 150.November 2017, pp. 176–193. DOI: 10.1016/j.oceaneng.2017.12.059.

Saouli, Y., M. Magnier, G. Germain, B. Gaurier, and P. Druault (2022). "Experimental charac- terisation of the waves propagating against current effects on the wake of a wide bathymetric obstacle". In: *18ème Journées de l'Hydrodynamique*. URL: https://jh2022.sciencesconf.org/413878.

Ting, F. C. and Y. K. Kim (1994). "Vortex generation in water waves propagating over a submerged obstacle". In: *Coastal Engineering* 24.1-2, pp. 23–49. DOI: 10.1016/0378-3839(94)90025-6.

Westerweel, J. and F. Scarano (2005). "Universal outlier detection for PIV data". In: *Experiments in Fluids* 39, pp. 1096–1100. DOI: 10.1007/s00348-005-0016-6.

Zaman, M. H., H. Togashi, and E. Baddour (2008). "Deformation of monochromatic water wave trains propagating over a submerged obstacle in the presence of uniform currents". In: *Ocean Engineering* 35.8-9, pp. 823–833. DOI: 10.1016/j.oceaneng.2008.01.018.

Zhang, X., R. Simons, J. Zheng, and C. Zhang (2022). "A review of the state of research on wave-current interaction in nearshore areas". In: *Ocean Engineering* 243, p. 110202. DOI: 10.1016/j.oceaneng.2021.110202.

Zhou, J., R. J. Adrian, S. Balachandar, and T. M. Kendall (1999). "Mechanisms for generating coherent packets of hairpin vortices in channel flow". In: *Journal of Fluid Mechanics* 387, pp. 353–396. DOI: 10.1017/S002211209900467X.